The Astrophysical Journal Letters, 833:L6 (6pp), 2016 December 10 doi:10.3847/2041-8205/833/1/L6

ALMA REVEALS POTENTIAL LOCALIZED DUST ENRICHMENT FROM MASSIVE STAR CLUSTERS IN II Zw 40

S. Michelle Consiglio[1], Jean L. Turner[1], Sara Beck[2], and David S. Meier[3]
[1] Department of Physics and Astronomy, University of California, Los Angeles, Los Angeles, CA 90095, USA; smconsiglio@ucla.edu
[2] Department of Physics and Astronomy, University of Tel Aviv, Ramat Aviv, Israel
[3] Department of Physics, New Mexico Institute of Mining and Technology, Socorro, NM 87801, USA
Received 2016 July 6; revised 2016 October 12; accepted 2016 October 13; published 2016 December 1

ABSTRACT

We present subarcsecond images of submillimeter CO and continuum emission from a local galaxy forming massive star clusters: the blue compact dwarf galaxy II Zw 40. At ∼0.″4 resolution (20 pc), the CO(3-2), CO(1-0), 3 mm, and 870 μm continuum maps illustrate star formation on the scales of individual molecular clouds. Dust contributes about one-third of the 870 μm continuum emission, with free–free accounting for the rest. On these scales, there is not a good correspondence between gas, dust, and free–free emission. Dust continuum is enhanced toward the star-forming region as compared to the CO emission. We suggest that an unexpectedly low and spatially variable gas-to-dust ratio is the result of rapid and localized dust enrichment of clouds by the massive clusters of the starburst.

Key words: galaxies: dwarf – galaxies: individual (IIZw40) – galaxies: star clusters: general – galaxies: starburst – submillimeter: galaxies

1. INTRODUCTION

Cycling of gas in galaxies drives galactic evolution; massive stars are important in this process because of their high luminosities, intense and hard radiation fields, and mass loss. In particular, concentrations of young, massive stars in clusters can rapidly create and expel large masses of metal-rich gas, which can potentially produce dust-enriched clouds (Turner et al. 2015). Dust-enriched gas can affect gas dynamics and interactions of young stars with their surroundings, determining the manner in which gas and dust are dispersed from massive clusters (Silich et al. 2004; Tenorio-Tagle et al. 2006; Krumholz & Matzner 2009; Murray et al. 2010; Draine 2011a; Kim et al. 2016). Differences between CO-derived and dust-derived masses in clouds of the LMC (Indebetouw et al. 2013; Galametz et al. 2016) suggest local variations in either the CO-to-H_2 conversion factor or in the gas-to-dust ratios (GTDs).

Previous submillimeter observations of modest spatial resolution blend regions of different ages and enrichment, which might explain globally uniform GTDs that are observed (Groves et al. 2015). The Atacama Large Millimeter/submillimeter Array (ALMA) has made possible high-resolution submillimeter maps that can resolve individual giant molecular clouds in local galaxies. It is now possible to test the assumption that gas and dust are well mixed on cluster scales.

II Zw 40 is a nearby ($D = 10$ Mpc), low-metallicity ($Z = 0.25\,Z_\odot$; Bordalo et al. 2009), blue compact dwarf galaxy. Although it hosts an exceedingly luminous "extragalactic H II region" (Sargent & Searle 1970; Thuan & Martin 1981; Kunth & Sargent 1983), it has very faint CO lines (Sage et al. 1992; Meier et al. 2001; Israel 2005). Its region of intense star formation (Beck et al. 2002, 2013; Wu et al. 2006; Vanzi et al. 2008; Kepley et al. 2014, 2016) contains at least two massive star clusters of $\sim 10^5$–$10^6\ M_\odot$ each (Beck et al. 2013). This "starburst" dominates the infrared spectrum of II Zw 40, which has an unusually warm peak at 60 μm (Vader et al. 1993). The dominance of the starburst makes II Zw 40 an excellent target for studying the effects of massive clusters on their environments.

We present here some of the first ALMA submillimeter λ3 mm and λ870 μm continuum and CO observations of an extragalactic star-forming region with massive young star clusters. We have mapped CO(3-2), CO(1-0), and continuum in II Zw 40. From these images we can study how well correlated CO and submillimeter dust continuum emission are on the scales of star-forming regions.

2. OBSERVATIONS

II Zw 40 (UGCA 116) was observed in ALMA Bands 3 and 7 as a Cycle 2 (Early Science) program (ID 2013.1.00122.S, PI: J. Turner). Band 7 observations took place on 2014 August 13 and December 13. A single field with an 18″ field-of-view centered on 05:55:42.620, +03.23.32.0 was observed with 2844 s on source. The (u, v) range covers ∼17–983 kλ; structures $\gtrsim$12″ are undersampled. This is not a problem for CO(3-2), since emission in individual channels is compact, nor for free–free emission. However, it could be an issue for dust, which traces both atomic and molecular gas. Band 3 observations took place on 2015 September 2 and 3, with 4927 s on source. Spectral resolution 244.141 kHz per channel resolves both CO(3-2) and CO(1-0) lines; we present the integrated intensity maps for emission >1.5σ. The (u, v) range for the 2.6 mm images covers ∼5–525 kλ, sampling structures up to ∼40″ ($\lesssim$1.9 kpc). Bandpass, phase, and flux were calibrated with J0607–0834, J0532 + 0732, and J0510 + 180, respectively. Data calibration using CASA followed the pipeline. Continuum emission was subtracted in the (u, v) plane before making line maps. All maps are convolved to a 0.″47 × 0.″4, PA = 51.°02 beam.

For the continuum maps, rms noise is 35μ Jy beam^{-1} for the 2 GHz band centered at 345.796 GHz ("870 μm") and 20 μJy beam^{-1} at 115.27 GHz ("3 mm"). The rms in a single 2 km s^{-1} Hanning-weighted channel is 1.5 mJy beam^{-1} for CO(1-0) maps and 1.6 mJy beam^{-1} for CO(3-2). The rms in the integrated intensity maps is 19 mJy beam^{-1} km s^{-1} in

CO(1-0) with a 1.5σ cutoff and 14 mJy beam^{-1} km s^{-1} for CO(3-2) with a 2.5σ cutoff. Single-dish fluxes from the literature are 1.4–4.6 Jy km s^{-1} for CO(1-0) in a 22″–24″ beam (Sage et al. 1992; Albrecht et al. 2004) and <6.7 Jy km s^{-1} for CO(3-2) (Meier et al. 2001; Israel 2005). We may detect up to half of the CO(1-0) single-dish flux, but this is unclear from the conflicting published values. We detect most, perhaps all, of the CO(3-2) single-dish flux, based on comparison with single-dish upper limits.

3. 3 mm FREE–FREE CONTINUUM, H II REGIONS, AND STAR FORMATION RATE IN II Zw 40

Free–free emission from the H II region dominates the 3 mm continuum of II Zw 40, shown in Figure 1(b); synchrotron and dust contributions are negligible. The 3 mm flux density for the inner 2″–3″ is $S_{3\rm mm} = 7.6 \pm 0.2$ mJy, with a peak of 1.67 ± 0.02 mJy beam^{-1} at R.A.: 05:55:42.614 decl.: 03.23.32.01 (J2000). Using opacity and recombination coefficient expressions from Draine (2011a, 2011b) we find $N_{\rm Lyc} = 1.25 \times 10^{50}\, T_4^{-0.51}\, \nu_{11}^{+0.118} \left(\frac{n_i}{n_p}\right) D_{\rm Mpc}^2\, S\,({\rm mJy})$, and for $T_e = 13{,}000$ K (Walsh & Roy 1993; Thuan & Izotov 2005), we obtain a Lyman continuum rate of $N_{\rm Lyc} = 8.3 \pm 0.2 \times 10^{52}$ s^{-1}. This is higher than estimated from centimeter-wave fluxes (Kepley et al. 2014), which can be caused by particularly dense ionized gas turning optically thin at millimeter wavelengths (Beck et al. 2002). Since dust competes with gas for UV photons the actual Lyman continuum rate will be higher than this value. Following Inoue et al. (2001), based on the observed $L_{\rm IR} \sim 1.9 \times 10^9\, L_\odot$ (Engelbracht et al. 2008, corrected for distance) and $N_{\rm Lyc}$, we estimate that 72% of the Lyman continuum photons end up ionizing hydrogen. The corrected Lyman continuum rate is therefore $N_{\rm Lyc}^{\rm corr} = 1.2 \pm 0.2 \times 10^{53}$ s^{-1}, corresponding to ~12,000 O stars, and a total stellar mass of ~1–2 × $10^6\, M_\odot$.

4. DUST AND MOLECULAR GAS IN II Zw 40

4.1. 870 μm *Continuum and Dust Distribution in II Zw 40*

The 870 μm continuum image is shown in Figure 1(a); total flux for the inner 6″ is $S_{870\,\mu{\rm m}} = 9.7 \pm 0.5$ mJy and the peak is 1.74 ± 0.06 mJy beam^{-1}. Hirashita (2013) found 13.6 ± 2.0 mJy, at 880 μm in a map with the Submillimeter Array. His peak flux of 8.5 mJy beam^{-1} in a 7″ beam is consistent with our total flux measurement for a region of the same size. This is ~10% of the flux in the single-dish JCMT-SCUBA maps, much of which arises in the extended H I tail (van Zee et al. 1998; Galliano et al. 2005; Hunt et al. 2005). The 870 μm continuum includes both dust and free–free emission. To map only the dust, we extrapolate the 3 mm free–free emission to 870 μm using the spectral index −0.118 (Draine 2011b). The total free–free flux density of $S_{870\,\mu{\rm m}}^{ff} = 6.7 \pm 0.2$ mJy is approximately two-thirds of the total. The remaining flux density is due to dust; we obtain $S_{870\,\mu m}^{\rm dust} = 3.0 \pm 0.5$ mJy. This value agrees with that of Kepley et al. (2016). The contribution of dust to the 3 mm continuum, for dust emissivity $\beta = 1.7$, is $S_{3\,\rm mm}^{\rm dust} < 0.1$ mJy.

Subtracting the scaled 3 mm free–free continuum from the 870 μm gives a map of the dust emission alone, shown in Figure 1(c). Dust is concentrated near the star formation in a region ~2″, or 100 pc in extent. Dust and ionized gas are not perfectly co-extensive: the peak flux in the 870 μm continuum is at 05:55:42.612, 03:23:32.02 (J2000), slightly (0.″14, or 7 pc) shifted from the 3 mm peak. Dust peaks include: a central peak, 0.38 mJy beam^{-1} (42.$^{\rm s}$604, 32.″06); western peak, 0.28 mJy beam^{-1} (42.$^{\rm s}$564, 31.″55); eastern peak, 0.32 mJy beam^{-1} (42.$^{\rm s}$649, 32.″11); and southern peak, 0.24 mJy beam^{-1} (42.$^{\rm s}$632, 31.″33). Dust fluxes in Table 1 differ from these because those are measured at CO(3-2) peaks.

4.2. Molecular Gas Distribution and Conditions

Integrated line images of CO(3-2) and CO(1-0) are shown in Figure 2. CO(3-2) traces dense (~10^4 cm^{-3}) gas, so the clouds in these images are dense clouds associated with the star formation. We restrict our discussion to the CO(3-2) and CO(1-0) in the dense, compact CO(3-2)-emitting clouds in this Letter; there may be more extended and diffuse clouds traced by CO(1-0) that may not be well represented in these images, while we recover most of the CO(3-2) flux (Section 2). CO(3-2) has been mapped previously by Kepley et al. (2016), but they did not detect CO(1-0) with ~3 times higher rms.

The overall integrated flux ratio of CO(3-2) and CO(1-0), R_{31}, where $I_{\rm line} = \int S_{\rm CO} dv$ (Jy km s^{-1}) is on average $R_{31} = I_{32}/I_{10} = (4.1 \pm 1.0/0.5 \pm 0.2) \sim 8$ and ranges from $R_{31} \sim$ 3–13 for CO(1-0) integrated intensity >1.5σ. The line ratio in thermal, optically thick gas is $R_{31} = 7.4$ for $T_{\rm gas} = 30$ K. The observed R_{31} is consistent with thermalized, warm gas. We have chosen the contours for the CO(3-2) in Figure 2 to be 7.4 times those of CO(1-0) to demonstrate the similarities in the maps at this value of R_{31}. The central extended cloud has significantly elevated $R_{31} \gtrsim 20$, as does the western cloud near the 3 mm continuum peak ($R_{31} \sim 10$), indicative of warmer gas directly associated with star formation. The observed II Zw 40 R_{31} cloud values are much higher than the galactic $\langle R_{31} \rangle = 1.6$ found in the JCMT survey of local SINGS galaxies (Wilson et al. 2012). Since we identify clouds based on CO(3-2) structure, it is not surprising that these clouds have higher than average R_{31} values. These CO(3-2)-emitting clouds are denser and warmer in II Zw 40 than typical spiral disk clouds, with log $(n/{\rm cm}^{-3}) \gtrsim$ 3.5–4.

4.3. Gas-to-Dust in II Zw 40

Figure 3 shows the gas and dust together. The CO-to-dust emission ratio varies significantly across the starburst region. The isolated CO cloud to the east is molecular gas-rich, with almost no dust emission. In contrast, the westernmost dust peak is relatively dust-rich, with weak CO. The ratio of CO(3-2) line flux to dust continuum flux varies from $S_{\rm CO32}/S_{870}^{\rm dust} \sim 1400$ km s^{-1} to $S_{\rm CO32}/S_{870}^{\rm dust} \sim 13{,}000$ km s^{-1}, almost an order of magnitude.

We calculate GTD by determining dust and gas masses separately. We focus on three regions 0.″6 in diameter: "Cloud W," coincident with the 3 mm free–free peak; "Cloud C," to the immediate east of the free–free peak; and "Cloud E," an isolated cloud to the east (Figure 2). Clouds E and W are similar in CO flux, but very different in dust emission. To obtain dust mass, we use a dust opacity calculated for an extended region in the LMC by Galliano et al. (2011), with $\kappa_{870\,\mu{\rm m}} = 0.9\,{\rm cm}^2\,{\rm g}^{-1}$ and $\beta = 1.7$. For Clouds C and W, we use the 33 K IRAS 60/100 color temperature (Engelbracht et al. 2008) and for the isolated Cloud E, we use $T_{\rm Dust} = 20$ K. We obtain a total dust mass

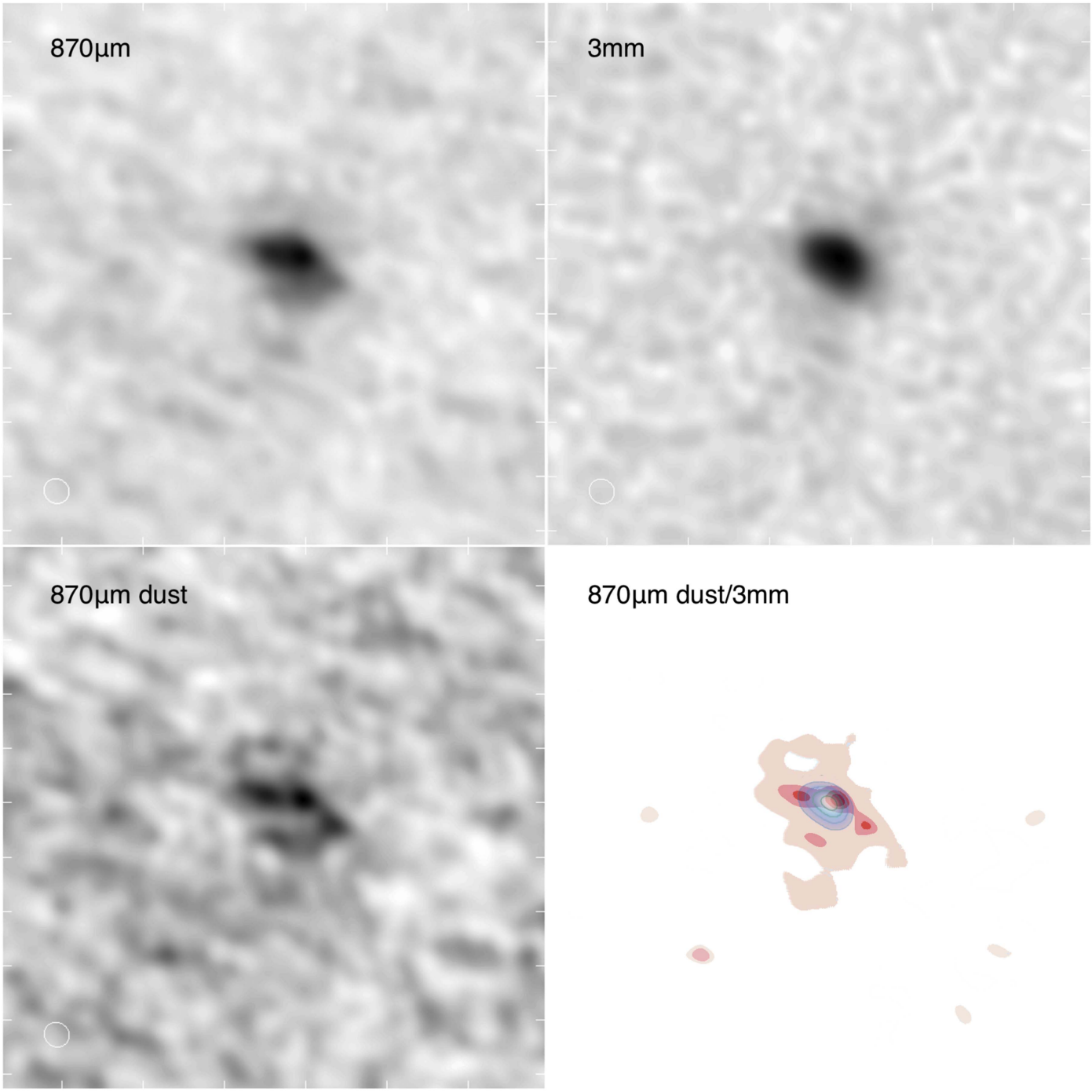

Figure 1. ALMA continuum and dust maps of II Zw 40. Beams are shown at the lower left and are all $0\farcs47 \times 0\farcs44$, PA 51°0. Tick marks, in white, are $0\farcs5$. (top left) 870 μm map. The rms is ~0.035 mJy beam^{-1}, and peak flux is 1.74 mJy beam^{-1} at 05:55:42.612, 03:23:32.02 (J2000). Total flux is 9.7 ± 0.5 mJy. (top right) 3 mm map. The rms is ~0.02 mJy beam^{-1}, and peak flux is 1.67 mJy beam^{-1} at 05:55:42.614, 03:23:32.01 (J2000). Total flux is 7.6 ± 0.2 Jy. (bottom left) 870 μm dust map (see the text). The rms is ~0.035 mJy beam^{-1}, and peak flux is 0.38 mJy beam^{-1}. Total dust flux is 3.0 ± 0.5 mJy. (bottom right) Schematic overlay of the 870 μm dust in orange with 3 mm free–free emission (H II region) in blue. Grayscale stretch is linear: from -1.5σ (white) to peak intensity (black).

for the central $5''$ of 17000 ± 5000 $M_\odot$(for $T = 33$ K). This may underestimate the true dust mass, since the SED peak is dominated by the warmest dust, which will not dominate the mass.

Gas masses are derived from CO(1-0) using the conversion factor, X_{CO}. Since the CO(1-0) detection is weak, we also include masses based on the CO(3-2) fluxes for comparison, using $R_{31} = 7.4$ to obtain the equivalent CO(1-0) flux. Because of excitation effects in CO(3-2), the CO(1-0) masses, while uncertain, are more reliable for using X_{CO}. We adopt the LMC conversion factor of $X_{CO} = 4.7 \times 10^{20}$ cm^{-2} (K km s^{-1}; Israel et al. 2003; Hughes et al. 2010). This value was obtained for more diffuse gas that is more likely to have CO-dark H_2; it could well overestimate the molecular gas in these dense clouds. Gas and dust masses and GTD calculated for the three Clouds E, C, and W, associated with CO(3-2) peaks, and for

Table 1
Gas, Dust, and GTD

Name	Position 05:55; +03:23	CO(1-0) (Jy km s^{-1})	CO(3-2) (Jy km s^{-1})	$\frac{(3-2)}{(1-0)}$ ratio	$M_{\rm gas}^{(1-0)}$ [a] ($10^4\,M_\odot$)	$M_{\rm gas}^{(3-2)}$ [a] ($10^4\,M_\odot$)	Dust Flux[b] (mJy)	$M_{\rm dust}$ [b] ($M_\odot$)	GTD[c] (1-0), (3-2)
Cloud W[d]	42.609, 32.03	0.06	0.71	12	13	21	0.34	1940	69, 110
Cloud E[d]	42.802, 32.482	0.055	0.52	9	12	16	<0.04	<450	>270, >350
Cloud C[d]	42.647, 32.264	0.045	0.93	21	10	28	0.29	1650	60, 170
Starburst[e]	42.695, 31.763	0.50	4.1	8	110	120	3.0	1.7×10^4	65, 72

Notes.
[a] From observed CO(1-0) flux and CO(3-2) flux with $R_{31} = 7.4$. Integrated line map rms is 19 and 14 mJy beam^{-1} km s^{-1} for CO(1-0) and CO(3-2) respectively. Mass includes He.
[b] Dust fluxes are measured from regions defined by the CO, not the dust peaks themselves, this underestimates the dust. Masses are estimated using a dust temperature of 33 K except for Cloud E, which is 20 K. Cloud E is an upper limit of 3σ.
[c] GTDs computed from CO(1-0) masses on the left and CO(3-2) masses on the right.
[d] Fluxes for 0.″6 diameter regions.
[e] For a 5″ diameter region.

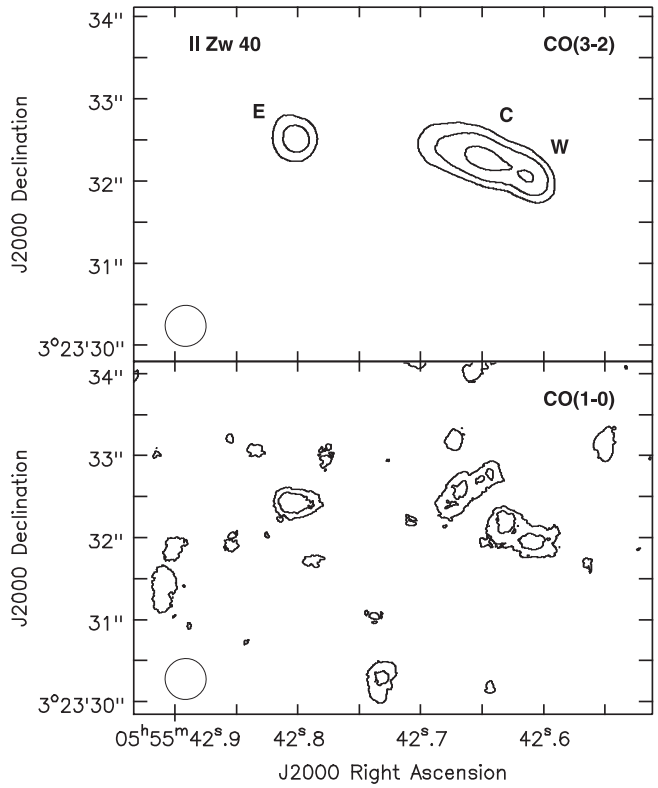

Figure 2. (top) CO(3-2) and (bottom) CO(1-0) integrated line intensity in II Zw 40. Contour levels are 0.37, 0.52, 0.74 Jy beam^{-1} km s^{-1} (∼26, 37, 53σ) for CO(3-2) and 0.05, 0.071, 0.10 Jy beam^{-1} km s^{-1} (∼2.6, 3.7, 5σ) for CO(1-0). Contour levels are 7.4 times higher for the CO(3-2) plot, as CO(3-2) is ∼7.4 times stronger than CO(1-0) for optically thick, thermal emission at 30 K.

the entire central 5″ starburst region are given in Table 1. The overall gas mass based on CO(1-0) is $M_{\rm gas} = 1.1 \times 10^6\,M_\odot$, including helium.

GTD is expected to scale with galactic metallicity, although with large scatter (Rémy-Ruyer et al. 2014). The metallicity of II Zw 40 is $12 + \log({\rm O/H}) \sim 8.1$, $\sim 0.25\,{\rm Z}_\odot$ (Bordalo et al. 2009), so the predicted GTD is ∼400–600. Only Cloud E approaches this value. The observed values of GTD ∼ 60–170 are far lower than expected for this low-metallicity galaxy.

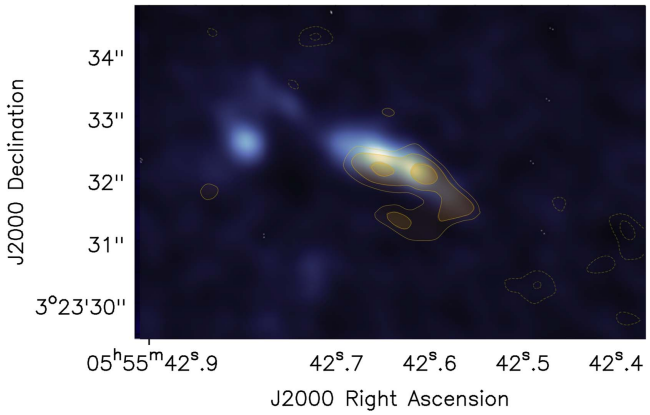

Figure 3. CO(3-2) emission (blue) with the dust map (orange) to show the relative spatial relation of the CO and dust emission. CO(3-2) map monochrome scale is from $3\sigma = 0.05$ to its peak, 0.85 (Jy beam^{-1} km s^{-1}). The dust continuum contours are ±0.15, 0.21, 0.3 mJy beam^{-1}, with negative contours dashed.

5. LOW AND SPATIALLY VARYING GAS-TO-DUST: GAS CONDITIONS OR STARBURST DUST PRODUCTION?

Derived GTD values in II Zw 40 are consistently lower than predicted from its metallicity. GTD also varies significantly across the region; from 70 in Cloud W to >270 in Cloud E, clouds similar in CO flux and size. There are several possible explanations for the variation. The missing gas mass is unlikely to be H I in these dense clouds. It is difficult to compare to the large beams of H I maps, but based on observed column densities (van Zee et al. 1998), we estimate that roughly 10% of the mass could be in H I in these compact clouds. Columns higher than this will become molecular gas. CO-dark H_2 is unlikely to contribute significantly in dense clouds (Langer et al. 2014); the adopted conversion factor has already accounted for this to some extent. $X_{\rm CO}$ variations could explain the variable GTD (as suggested for the LMC; Galametz et al. 2016). For the entire region to have the same GTD as Cloud E would require $X_{\rm CO} = 35$–$45 \times 10^{20}\,{\rm cm}^{-2}({\rm K\,km\,s}^{-1})$ in dense clouds where CO-dark H_2 is not expected, and it requires that $X_{\rm CO}$ vary by a factor of 4–10 across a region of $\lesssim$200 pc extent. High values of $X_{\rm CO}$ have been inferred in other low-metallicity galaxies, but under the assumption of a uniform GTD (Shi et al. 2014, 2015), which we argue below is

questionable. We also note the apparent contradiction in any model relying on CO-dark H_2: to explain these results requires extinction be lowest in clouds where dust emission is strongest.

We favor instead for II Zw 40 a model in which the GTD is low and variable because the starburst has enriched the surrounding clouds in metals and dust. Massive clusters such as those in II Zw 40 contain the most massive O stars (Smith et al. 2016) that lose most of their mass within a few Myr (Ekström et al. 2012). Both the Geneva high-mass-loss stellar models and the rotating models used in Starburst99 (Leitherer et al. 1999, 2014) predict metal (CNOSiMg) yields of up to 60,000 $M_\odot$ for clusters of this luminosity ($\sim 2 \times 10^9\, L_\odot$) that are 3 Myr or older. If half of this metal yield were in the form of dust, as in the Galaxy (Jenkins 2009), then 30,000 $M_\odot$ of dust could be present. We infer a total dust mass that is half this amount. In this scenario, the dominant source of dust is production in the stars of the massive clusters, and the contribution of dust from the natal clouds is small. This explains the contrast in GTD between Cloud W, which has been enriched by the massive clusters, and Cloud E, which has little star formation. This theory is also consistent with the significant spatial variations seen in the inferred oxygen abundances within this region by Bordalo et al. (2009). Enrichment is a natural and expected result of the stellar evolution of large clusters containing O stars.

Localized dust enrichment also provides an explanation for the spatial distribution of the dust (Draine 2011a; Kim et al. 2016). In luminous clusters, radiation pressure can cause the dust to drift relative to the gas, by ~ 1 km s^{-1}. This could explain the slight offset of the main dust peak ($\sim$10 pc) from the radio continuum peak and presence of dust mostly outside the H II region. Regions of dust emission without gas or continuum, such as the westernmost dust peak, may signal the presence of older clusters which no longer have H II regions. At a sound speed of 10 km s^{-1}, 100 Myr is required to cover the observed dust-emitting region; the presence of radio continuum emission suggests that these clusters are much younger. The starburst in II Zw 40 is young enough that the cluster-enriched gas has not had time to fully disperse.

These observations of II Zw 40 suggest that dust enrichment from massive clusters can be rapid and localized in starburst galaxies. This could explain why very high values of $X_{\rm CO}$ are inferred when Galactic GTD are assumed (e.g., Shi et al. 2014, 2015). Localized enrichment by massive star clusters may also explain why dusty galaxies, or dusty regions within galaxies, are seen so early in the universe (Watson et al. 2015).

6. SUMMARY AND CONCLUSIONS

We present ALMA continuum maps at 3 mm and 870 μm and integrated intensity images of the CO(3-2) and CO(1-0) lines in the blue compact dwarf galaxy II Zw 40, at a resolution of $\sim 0\farcs4$ ($\sim$20 pc). Based on a 3 mm continuum flux of 7.6 ± 0.2 mJy, we obtain a Lyman continuum rate of $N_{\rm Lyc}^{\rm corr} = 1.2 \pm 0.2 \times 10^{53}$ s^{-1} with $\sim$72% of the uv photons ionizing the gas. From 3 mm and 870 μm continuum maps, we construct a dust-only continuum map. For a dust flux of $S_{870\,\mu{\rm m}}^{\rm dust} = 3.0 \pm 0.5$ mJy, we estimate a dust mass of $\sim 17{,}000 \pm 5000\, M_\odot$, for $T_{\rm dust} = 33$ K. While CO(1-0) emission is weak, CO(3-2) and CO(1-0) line emission maps show similar structure and are consistent with warm, thermalized gas: CO(3-2) integrated fluxes are $\sim$3–13 times stronger than the CO(1-0). Adopting an LMC $X_{\rm CO} = 4.7 \times 10^{20}\,{\rm cm}^{-2}({\rm K\,km\,s}^{-1})^{-1}$, we estimate a gas mass of $M_{\rm gas} = 1.1 \times 10^6\, M_\odot$, including helium, comparable to the masses of the star clusters. The CO(3-2) extends over $4''$ (200 pc), significantly larger than the free–free emission, while the dust is concentrated to the immediate $\sim 2''$ (100 pc) vicinity of the starburst.

The ratio of CO(3-2) line flux to dust continuum flux varies from $S_{\rm CO32}/S_{870}^{\rm dust} \sim 1400$ km s^{-1} to $S_{\rm CO32}/S_{870}^{\rm dust} \sim 13{,}000$ km s^{-1} across the source. Some of this variation is due to CO(3-2) excitation, but much of it is due to gas column variations. For values of $X_{\rm CO}$ and dust opacity from the LMC, we find the gas-to-dust ratio, based on CO(1-0) fluxes, is unexpectedly low and variable across the 200 pc region: GTD $\sim$ 60–70 in the $0\farcs6$ regions ($\sim$50 pc) adjacent to the starburst, but GTD > 270 in a similar, but isolated and quiescent cloud $\lesssim$200 pc to the east. We argue that a low and variable GTD ratio in II Zw 40 is a result of dust produced by the O stars within the massive star clusters, an example of localized dust enrichment by a starburst that has not yet had time to disperse.

This Letter makes use of the following ALMA data: ADS/JAO.ALMA#2013.1.00122.S. ALMA is a partnership of ESO (representing its member states), NSF (USA) and NINS (Japan), together with NRC (Canada), NSC and ASIAA (Taiwan), and KASI (Republic of Korea), in cooperation with the Republic of Chile. The Joint ALMA Observatory is operated by ESO, AUI/NRAO and NAOJ. The National Radio Astronomy Observatory (NRAO) is a facility of the National Science Foundation operated under cooperative agreement by Associated Universities, Inc. Support for this work was provided by the NSF through award GSSP SOSPA2-016 from the NRAO to SMC and grant AST 1515570 to JLT, and by the UCLA Academic Senate through a COR seed grant. We thank the anonymous referee for thorough comments that aided our manuscript.

Facility: ALMA.

REFERENCES

Albrecht, M., Chini, R., Krügel, E., Müller, S. A. H., & Lemke, R. 2004, A&A, 414, 141
Beck, S., Turner, J., Lacy, J., Greathouse, T., & Lahad, O. 2013, ApJ, 767, 53
Beck, S., Turner, J., Langland-Shula, L., et al. 2002, AJ, 124, 2516
Bordalo, V., Plana, H., & Telles, E. 2009, ApJ, 696, 1668
Draine, B. T. 2011a, ApJ, 732, 100
Draine, B. T. 2011b, in Physics of the Interstellar and Intergalactic Medium, ed. B. T. Draine (Princeton, NJ: Princeton Univ. Press), 95
Ekström, S., Georgy, C., Eggenberger, P., et al. 2012, A&A, 537, A146
Engelbracht, C. W., Rieke, G. H., Gordon, K. D., et al. 2008, ApJ, 678, 804
Galametz, M., Hony, S., Albrecht, M., et al. 2016, MNRAS, 456, 1767
Galliano, F., Hony, S., Bernard, J.-P., et al. 2011, A&A, 536, A88
Galliano, F., Madden, S. C., Jones, A. P., Wilson, C. D., & Bernard, J.-P. 2005, A&A, 434, 867
Groves, B. A., Schinnerer, E., Leroy, A., et al. 2015, ApJ, 799, 96
Hirashita, H. 2013, MNRAS, 429, 3390
Hughes, A., Wong, T., Ott, J., et al. 2010, MNRAS, 406, 2065
Hunt, L., Bianchi, S., & Maiolino, R. 2005, A&A, 434, 849
Indebetouw, R., Brogan, C., Chen, C.-H. R., et al. 2013, ApJ, 774, 73
Inoue, A. K., Hirashita, H., & Kamaya, H. 2001, ApJ, 555, 613
Israel, F. P. 2005, A&A, 438, 855
Israel, F. P., de Graauw, T., Johansson, L. E. B., et al. 2003, A&A, 401, 99
Jenkins, E. B. 2009, ApJ, 700, 1299
Kepley, A. A., Leroy, A. K., Johnson, K. E., Sandstrom, K., & Chen, C.-H. R. 2016, ApJ, 828, 50
Kepley, A. A., Reines, A. E., Johnson, K. E., & Walker, L. M. 2014, AJ, 147, 43

Kim, J.-G., Kim, W.-T., & Ostriker, E. C. 2016, ApJ, 819, 137
Krumholz, M. R., & Matzner, C. D. 2009, ApJ, 703, 1352
Kunth, D., & Sargent, W. L. W. 1983, ApJ, 273, 81
Langer, W. D., Velusamy, T., Pineda, J. L., Willacy, K., & Goldsmith, P. F. 2014, A&A, 561, A122
Leitherer, C., Ekström, S., Meynet, G., et al. 2014, ApJS, 212, 14
Leitherer, C., Schaerer, D., Goldader, J. D., et al. 1999, ApJS, 123, 3
Meier, D. S., Turner, J. L., Crosthwaite, L. P., & Beck, S. C. 2001, AJ, 121, 740
Murray, N., Quataert, E., & Thompson, T. A. 2010, ApJ, 709, 191
Rémy-Ruyer, A., Madden, S. C., Galliano, F., et al. 2014, A&A, 563, A31
Sage, L. J., Salzer, J. J., Loose, H.-H., & Henkel, C. 1992, A&A, 265, 19
Sargent, W. L. W., & Searle, L. 1970, ApJ, 162, 155
Shi, Y., Armus, L., Helou, G., et al. 2014, Natur, 514, 335
Shi, Y., Wang, J., Zhang, Z.-Y., et al. 2015, ApJL, 804, L11
Silich, S., Tenorio-Tagle, G., & Rodríguez-González, A. 2004, ApJ, 610, 226
Smith, L. J., Crowther, P. A., Calzetti, D., & Sidoli, F. 2016, ApJ, 823, 38
Tenorio-Tagle, G., Muñoz-Tuñón, C., Pérez, E., Silich, S., & Telles, E. 2006, ApJ, 643, 186
Thuan, T. X., & Izotov, Y. I. 2005, ApJS, 161, 240
Thuan, T. X., & Martin, G. E. 1981, ApJ, 247, 823
Turner, J. L., Beck, S. C., Benford, D. J., et al. 2015, Natur, 519, 331
Vader, J. P., Frogel, J. A., Terndrup, D. M., & Heisler, C. A. 1993, AJ, 106, 1743
van Zee, L., Skillman, E., & Salzer, J. 1998, AJ, 116, 1186
Vanzi, L., Cresci, G., Telles, E., & Melnick, J. 2008, A&A, 486, 393
Walsh, J. R., & Roy, J. R. 1993, MNRAS, 262, 27
Watson, D., Christensen, L., Knudsen, K. K., et al. 2015, Natur, 519, 327
Wilson, C. D., Warren, B. E., Israel, F. P., et al. 2012, MNRAS, 424, 3050
Wu, Y., Charmandaris, V., Hao, L., et al. 2006, ApJ, 639, 157